5. D. A. Kring, *GSA Today* **8**, 2 (2000).
6. C. B. Officer, A. Hallam, C. L. Drake, J. D. Devine, *Nature* **326**, 143 (1987).
7. C. Hofmann, G. Feraud, V. Courtillot, *Earth Planet. Sci. Lett.* **180**, 13 (2000).
8. J. Smit, A. J. T. Romein, *Earth Planet. Sci. Lett.* **74**, 155 (1985).
9. T. D. Herbert, S. D'Hondt, *Earth Planet. Sci. Lett.* **99**, 263, (1990).
10. A. Montanari, *J. Sed. Petrol.* **61**, 315 (1991).
11. G. Keller, B. Barrera, B. Schmitz, E. Mattson, *Geol. Soc. Am. Bull.* **105**, 979 (1993).
12. M. Ozima, M. Takayanagi, S. Zashu, S. Amari, *Nature* **311**, 449 (1984).
13. K. A. Farley, S. G. Love, D. B. Patterson, *Geochim. Cosmochim. Acta* **61**, 2309 (1997).
14. D. B. Patterson, K. A. Farley, B. Schmitz, *Earth Planet. Sci. Lett.* **163**, 315 (1998).
15. Supplementary data are available on *Science* Online at www.sciencemag.org/cgi/content/full/291/5510/1952/DC1.
16. The Ain Settara section (STW) is ~50 km south of the El Kef section. The thickness of the K-T clay in the two sections is approximately equal, and the STW section has been correlated to the El Kef stratotype (J. Kirschvink, personal communication) (*17*).
17. C. Dupuis, E. Steurbaut, M. F. Matmati, abstracts presented at the International Workshop on Cretaceous-Tertiary Transition, Tunis, Tunisia, 13 to 16 May 1998.
18. S. Mukhopadhyay, K. A. Farley, A. Montanari, *Geochim. Cosmochim. Acta*. **65**, 653 (2001).
19. K. A. Farley, in *Accretion of Extraterrestrial Matter Throughout Earth's History*, B. Peucker-Ehrenbrink, B. Schmitz, Eds. (Kluwer, Dordrecht, Netherlands, in press).
20. A. O. Nier, D. J. Schlutter, *Meteoritics* **25**, 263 (1990).
21. D. B. Patterson, K. A. Farley, M. D. Norman, *Geochim. Cosmochim. Acta* **63**, 615, (1999).
22. K. A. Farley, A. Montanari, E. M. Shoemaker, C. S. Shoemaker, *Science* **280**, 1250 (1998).
23. M. V. Sykes, A. A. Lebofsky, D. M. Hunter, F. Low, *Science* **232**, 1115 (1986).
24. P. R. Weissman, *Ann. N.Y. Acad. Sci.* **822**, 67 (1997).
25. S. J. Kortenkamp, S. F. Dermott, *Science* **280**, 874 (1998).
26. At STW, He measurements were made from the Ir-rich layer (*17*), and 20 and 80 mm above this layer (Table 1). On the basis of the three measurements, we assign an average [^{3}He] of 20 $\times$ 10^{-15} cm^3 standard temperature and pressure (STP) g^{-1} for the boundary clay. ^{3}He/^{4}He ratios at STW (Table 2) are close to typical crustal ratios of 0.03 R_A (*19*), suggesting that 20% or less of [^{3}He] is extraterrestrial. A reasonable lower limit of the crustal end-member is 0.015 R_A (*19*), and we adopted this value for calculating $[^3He]_{Et}$. Hence, the computed duration of the boundary event from STW is an upper limit.
27. J. Smit, *Annu. Rev. Earth Planet. Sci.* **27**, 75 (1999).
28. L. Becker, R. J. Poreda, T. E. Bunch, *Proc. Natl. Acad. Sci. U.S.A.* **97**, 2979 (2000).
29. The total ^{3}He contribution from the bolide in the Italian K-T clay cannot exceed the ^{3}He concentration of 15 $\times$ 10^{-15} cm^3 STP g^{-1} in the fallout lamina at STW, which is <8% of the measured ^{3}He in the Italian K-T clays.
30. K. J. Hsu, J. A. McKenzie, Q. X. He, *Geol. Soc. Am. Spec. Pap.* **190**, 317 (1982).
31. S. D'Hondt, P. Donaghay, J. C. Zachos, D. Luttenberg, M. Lindinger, *Science* **282**, 276 (1998).
32. J. Smit, *Geol. Mijnbouw* **69**, 187 (1990).
33. S. C. Cande, D. V. Kent, *J. Geophys. Res.*, **100**, 6093 (1995).
34. We thank J. Kirschvink and T. Raub for providing the STW samples (sample collection funded by NSF EAR9807741) and F. Robaszynski for discussion on the STW section. Funded by NASA and the David and Lucille Packard Foundation.

16 November 2000; accepted 1 February 2001

REPORTS

Continuous Mantle Melt Supply Beneath an Overlapping Spreading Center on the East Pacific Rise

Robert A. Dunn,[1,2]* Douglas R. Toomey,[1] Robert S. Detrick,[3] William S. D. Wilcock[4]

Tomographic images of upper mantle velocity structure beneath an overlapping spreading center (OSC) on the East Pacific Rise indicate that this ridge axis discontinuity is underlain by a continuous region of low *P*-wave velocities. The anomalous structure can be explained by an approximately 16-kilometer-wide region of high temperatures and melt fractions of a few percent by volume. Our results show that OSCs are not necessarily associated with a discontinuity in melt supply and that both OSC limbs are supplied with melt from a mantle source located beneath the OSC. We conclude that tectonic segmentation of the ridge by OSCs is not the direct result of magmatic segmentation at mantle depths.

The discovery that fast-spreading oceanic ridges are structurally (*1, 2*) and chemically (*3, 4*) segmented between transform offsets has led to competing hypotheses for the origin of ridge segmentation (*5, 6*). Central to this controversy is the question of the cause of OSCs. OSCs are segment boundaries characterized by the overlap of two ridge segments which offset the axial neovolcanic zone by 0.5 to 15 km. The larger OSCs consist of two distinct ridge limbs that surround a central basin (*7*). Unlike transform offsets, which are stationary with respect to the ridge, OSCs migrate along axis and, in doing so, individual limbs may propagate, recede, or be rafted off to the side of the rise, leaving behind a distinctive seafloor morphology and disrupted magnetic lineations (*7–9*). Studies of the wakes of OSCs indicate that these ridge discontinuities are unstable on a time scale as short as 50,000 years (*8, 9*). The structural evolution of OSCs has led some to speculate that their origin is the result of fluctuations in axial magmatic processes (*7, 10*). By this view, OSCs occur above regions of reduced magma supply, perhaps at the boundary between two widely separated regions of mantle upwelling (*11*). This model asserts that OSCs are the result of converging, but misaligned episodes of lateral (along the ridge axis) magma injection, such that each limb has a separate source of mantle-derived magma. In contrast, an opposing model states that OSCs are the result of tectonic processes, such as those resulting from changes in the kinematics of spreading (*1, 12*). In this hypothesis, mantle upwelling is approximately two-dimensional or sheet-like, and the magma supply beneath the OSC is uninterrupted. Thus, the morphologically distinct limbs of an OSC share a common source of magma (*1*).

To test these competing models of magma supply to fast-spreading ridges, we conducted a seismic experiment along the East Pacific Rise (EPR) between the Clipperton and Siqueiros transforms (Fig. 1). Here, we report on a subset of the data which allows imaging of lateral variations in shallow mantle *P*-wave velocity structure beneath an 80-km-long section of the rise that includes the 9°03′N OSC. This OSC and associated ridge segments have been well studied by geophysical mapping (*8, 9, 13, 14*), petrologic and geochemical analysis of seafloor basalts (*3*), and multichannel seismic (MCS) experiments (*15–17*). The OSC consists of two north-south trending ridge segments that overlap by 27 km, are offset by 8 km, and enclose a central basin. In general, normal (N-type) mid-ocean ridge basalts (MORBs) have been recovered from the northern segment of the rise, and enriched-type MORBs have been recovered from the southern segment (*3*), leading some to infer that this ridge discontinuity separates two physically and chemically distinct sources of magma.

The seismic experiment consisted of an array of 15 ocean-bottom instruments that

[1]Department of Geological Sciences, University of Oregon, Eugene, OR 97403–1272, USA. [2]Department of Geological Sciences, Brown University, Providence, RI 02912–1846, USA. [3]Department of Geology and Geophysics, Woods Hole Oceanographic Institute, Woods Hole, MA 02543, USA. [4]School of Oceanography, University of Washington, Seattle, WA 98195–7940, USA.

*To whom correspondence should be addressed at Brown University. E-mail: Robert_Allen_Dunn@brown.edu

recorded the crustal and mantle travel times of 1327 airgun shots (Fig. 1) (*18*). The experiment geometry is designed to image the velocity structure of the uppermost mantle, within ~4 km of the Moho, in a horizontal plane that extends ~15 km to either side of the rise axis and 40 km to the north and south of the OSC. Our analysis includes the delay times of 2977 mantle refractions (*Pn*), 2831 crustal refractions (*Pg*), and 802 reflections from the Moho (*PmP*) (*19*). The crustal phases constrain the three-dimensional structure of the off-axis crust, including crustal thickness, along the crustal portion of the *Pn* ray paths.

To provide a starting model for tomographic inversions, we first constructed a three-dimensional crustal model from the results of Canales *et al.* (*20*), which constrain velocity variations in the crust and crustal thickness beneath the outer refraction lines of our experiment (*21*). This model was used as a starting model for a three-dimensional inversion for crustal structure that included *Pg* and *PmP* data whose ray paths traveled both along and between the inner and outer refraction lines. The resulting crustal model (normalized χ^2 misfit of ~1), to which was added a constant-velocity (7.8 km s^{-1}) isotropic mantle, then became the starting model for inversions that included the crustal and mantle *Pn* data. The starting model includes off-axis crustal structure but does not include subaxial crustal structure, which is not traversed by *Pn* waves.

The *Pn* travel-time delays, calculated with respect to the starting model, indicate the presence of a mantle low-velocity zone (LVZ) and anisotropic wave propagation beneath the rise. When plotted as a function of the point at which a *Pn* ray crosses the rise axis, the *Pn* delays indicate that the LVZ is continuous beneath the OSC but varies in width and/or magnitude (Fig. 2). When plotted as a function of ray-path azimuth (θ), the *Pn* delays display a cos(2θ) dependence (Fig. 2C), a signal consistent with velocity anisotropy due to the alignment of the crystallographic *a* axes of olivine grains in the spreading direction (*22, 23*).

Images of the mantle seismic structure are constructed using a nonlinear tomographic method (*24–27*) that allows the user to explore the solution space and data misfit by adjusting constraints on model smoothness and the relative importance of isotropic versus anisotropic parameters. Purely isotropic solutions do not provide adequate fits to the data ($\chi^2_{Pn} \geq 3$) and cos(2θ) trends remain in the data residuals. Models with 5 to 7% mantle anisotropy, with the fast axis of anisotropy everywhere aligned within a few degrees of the spreading direction, provide the best fit to the *Pn* data ($\chi^2_{Pn} \sim 1$, >95% variance reduction) and remove the cos(2θ) trend from the residuals. In contrast to a similar study (*25*), we found only moderate trade-off between the magnitude of the anisotropy and the average upper-mantle velocity (because of the greater density and coverage of the *Pn* rays used in this experiment versus the earlier study). Small lateral variations in the fast-axis azimuth or magnitude of anisotropy are permitted although not required by the data (*28*). Further tests (*29*) indicate that reasonable errors in the crustal thickness of the starting model produce a negligible error (<0.05 km s^{-1}) in the mantle images.

The mantle velocity structure is characterized by a subaxial zone of low velocities that is continuous beneath the OSC and which underlies both ridge limbs (Fig. 3A). The LVZ extends ~8 km to either side of the rise axis and is up to 0.7 km s^{-1} slower than off-axis mantle velocities. The width of the LVZ (defined by the −0.2 km s^{-1} contour line in Fig. 3A) and the absolute velocities therein are similar to values for a mantle LVZ beneath the EPR near 9°30′N [~20 km north of this experiment (*25*)]. Synthetic checkerboard models with block widths of ≥4 km are well reconstructed beneath the OSC (Fig. 3, B and C), indicating that model resolution is sufficient to discriminate between OSC limbs that are underlain by a single LVZ versus those with two distinct LVZs. In addition, the *Pn* data require the LVZ to extend at least 4 km beneath the Moho; otherwise, seismic waves would simply propagate beneath the LVZ and not be influenced by it (*25*).

Although the mantle LVZ to the south

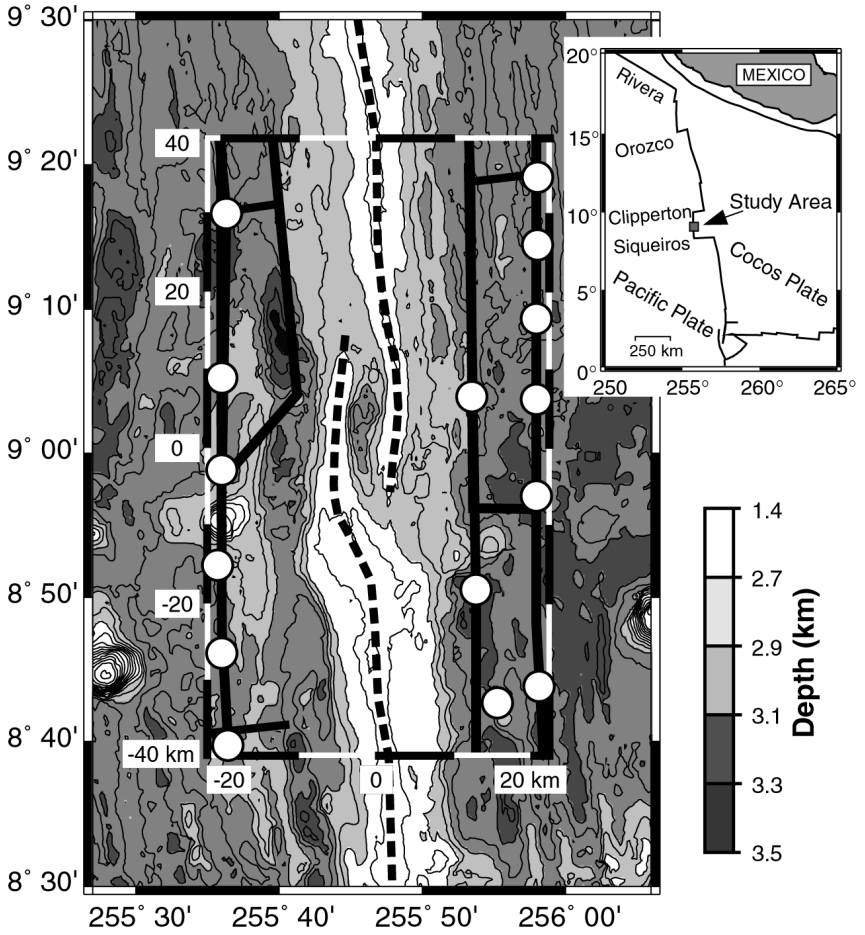

Fig. 1. Location and geometry of the seismic experiment. Bathymetry is contoured at 100-m intervals, and the dashed lines indicate the location of the rise axis. The local full spreading rate is ~115 mm $year^{-1}$. The area of seismic imaging is shown by the black-and-white dashed box. An array of ocean-bottom instruments, depicted as white circles, recorded compressional-wave travel times from airgun shots that occurred every 400 to 500 m along the heavy black lines. For mantle imaging, the data set contains mantle refraction travel times, *Pn*, observed as first arrivals for shot-receiver paths connecting instruments on one side of the rise axis and lines of shots on the other side of the rise axis, and for paths that connect shots and receivers along the rise-parallel refraction lines. The crustal legs of the *Pn* paths are situated well away from the axis of the rise, thus avoiding the complex structure of the crustal magmatic system.

of the OSC is generally centered beneath the rise axis, to the north it is located westward of the rise axis by 3 to 5 km (Fig. 3A). This offset coincides with a westward displacement of the upper crustal melt lens observed in seismic reflection studies (*16, 17*) and with cross-axis asymmetries in both the mantle Bouguer gravity anomaly (*30*) and the morphology of the rise (*13*). Along-axis variations in the mantle velocity structure are required by the data; models with no along-axis variation provide poor data misfits ($\chi^2_{Pn} \sim 12$). In the along-axis direction, there are local peaks in the magnitude and width of the LVZ which correspond with peaks observed in the trend of the delay-time data (Fig. 2B). The largest of these peaks is situated just south of the OSC and is coincident with a large negative mantle-Bouguer gravity anomaly (*30*) and the broadest and highest standing section of the rise in our study area (*13*). North of the OSC, a smaller peak is located between the OSC and a small offset in the ridge [a deviation in axial linearity, or deval (*3*), at ~9°17′N]. In addition, two adjacent peaks underlie the OSC.

Our results indicate that an axially continuous region of melt resides in the mantle beneath the rise. The magnitude of the LVZ is too large to be caused by temperature alone [such a magnitude would require temperature variations of 1500°C (*26*)]. If mantle temperature variations are <200°C (*31*), then most of the velocity anomaly is due to melt. Assuming that melt resides in randomly oriented pockets of which 25% are tubules and 75% are thin disk shapes, as suggested by laboratory studies (*32*), melt fractions are ~2 to 3% by volume beneath the rise axis and vary along the axis by a factor of 1.5. There may be three times this amount of melt if instead it resides in thick-shaped pockets (*26*). These estimates represent an average over the scale of the model resolution (~2 to 4 km) and are similar in value to estimated melt fractions beneath the 9°30′N area (*25, 26*).

North of the OSC, our results indicate that the rise axis is displaced eastward of the mantle melt supply by as much as 5 km. We suggest that the plate boundary/neovolcanic zone has been displaced eastward of the source of mantle melt by a recent change in the spreading direction and an associated counterclockwise rotation of the northern plate boundary (*8, 9*). This displacement explains the relative westward offset of the shallow crustal melt lens seen in seismic reflection data (*16, 17*), and the cross-axis asymmetries of the mantle-Bouguer gravity anomaly (*30*) and morphology of the rise (*13*). As suggested by (*16*), the increase in axial depth as the OSC is approached from the north, which has been attributed to a decrease in magma supply near the OSC (*7*), may instead be the result of a southward increase in the offset between the locus of mantle melt and the neovolcanic zone. By this view, some variations in the width of the shallow melt lens, the morphology of the axial high, the axial depth, and perhaps the degree of crystal fractionation of MORB melts can be attributed to cross-axis misalignment between mantle melt delivery and the neovolcanic zone.

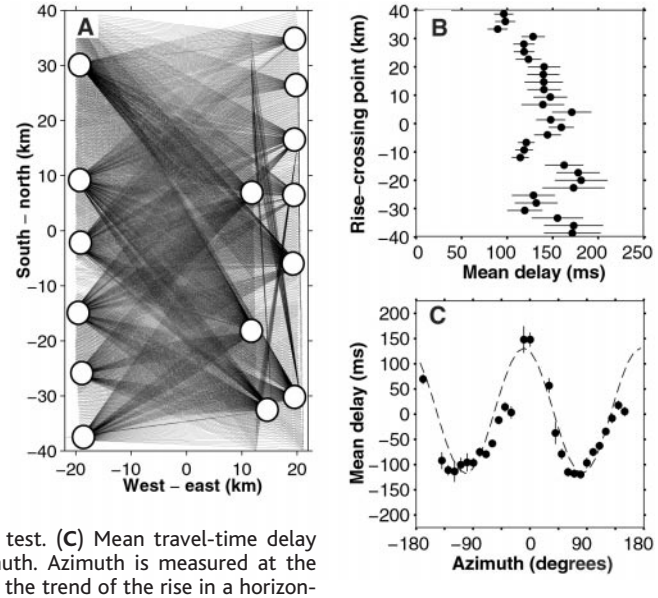

Fig. 2. (**A**) *Pn* ray paths in map view illustrate density of coverage and angular distribution of rays. (**B**) *Pn* delay times calculated with respect to the starting model (effects of path length, crustal structure, and an isotropic mantle are removed). Mean travel-time delay is plotted versus a ray path's rise-crossing point. The data have been sorted into bins by their individual rise-crossing points; each point represents the mean value of a 2-km-length bin, and the horizontal bars represent the 95% confidence interval of an estimated mean, as determined by Student's *t* test. (**C**) Mean travel-time delay versus source-receiver azimuth. Azimuth is measured at the receiver and clockwise from the trend of the rise in a horizontal plane (−98° and 82° are the rise perpendicular directions). The data are binned by azimuth so that each point represents the mean delay of a 10°-wide bin. The delays have also been corrected for the effect of a mantle-level low-velocity region with a 20-km width centered beneath the rise (a two-dimensional, axially invariant structure).

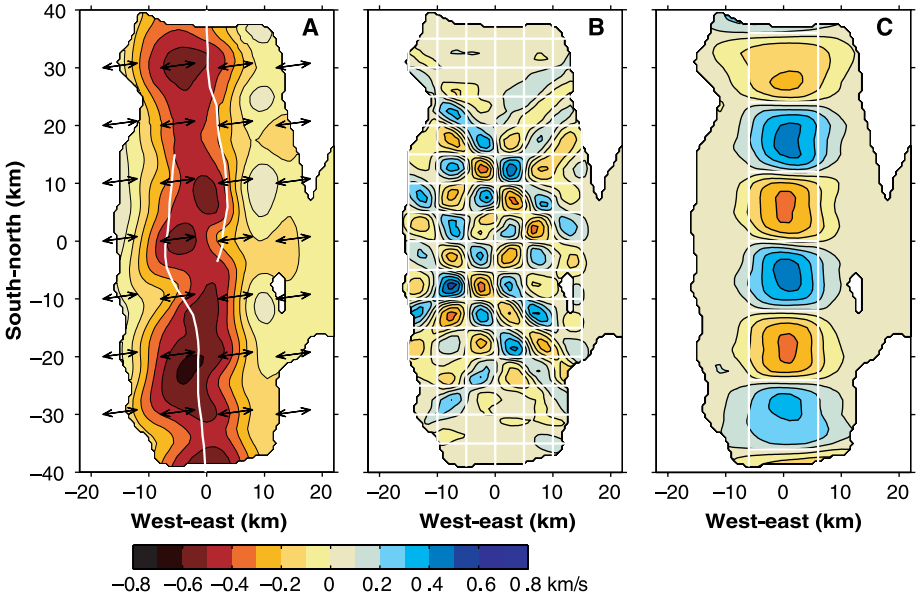

Fig. 3. (**A**) Results of tomographic imaging at a depth of 7 km, derived from *Pn* delay times. Contours indicate velocity perturbations with respect to 7.8 km s^{-1}. The region shown corresponds to the area with a good population of *Pn* rays. Arrows indicate the orientation of the fast-axis of seismic anisotropy (6% magnitude). The white lines indicate the position of the ridge axes. Resolution tests provide estimates of the (**B**) fine- and (**C**) large-scale model resolution beneath the rise. Test models contained synthetic anomalies of 2 to 6 km half width, extending vertically throughout the mantle; element velocities varied by ±0.3 km s^{-1}. Images are horizontal slices taken at 7 km depth through the reconstructed model for the case with 2.5- and 6-km half-width elements. White lines indicate the original positions of the anomalies. In the northern and southern latitudes of the model, where azimuthal ray coverage is incomplete, only relatively larger scale anomalies are resolvable.

Our results support the hypothesis that the volcanic segmentation of the rise, as characterized by small offsets of the neovolcanic zone (devals), is the result of along-axis fluctuations in the underlying magma plumbing system on a scale of 10 to 20 km (*3, 24–26, 33–37*). The 10- to 20-km scale of variability in mantle seismic structure observed here (Fig. 3A) is similar in scale to correlated variations observed in seafloor morphology [i.e., devals (*3, 13, 35*)], mantle and crustal seismic structure (*24–26, 33, 34*), geology (*3, 35*), and potential field anomalies (*36, 37*) along other parts of the EPR. Collectively, these results indicate that crustal-level magma chambers beneath fast spreading ridges are replenished at closely spaced intervals along the rise. These results are not compatible with models in which significant redistribution of melt occurs through along-axis flow at shallow levels (over tens of km), nor with models in which melt is supplied to the OSC from distal sources located along each ridge segment.

Images of the mantle velocity structure show that the 9°03′N OSC is not associated with a discontinuity in melt supply from the underlying mantle, that both limbs of the OSC share a common mantle-level source of melt, and that the thermal structure of the ridge is continuous beneath the OSC. Our study complements recently reported seismic observations that reveal shallow crustal magma lenses beneath both limbs of the OSC and a LVZ in the crust beneath the OSC (*16, 17, 38*). Although the crustal magma lenses are significantly offset from each other across the OSC, the geometry of the inferred magma distribution suggests that melt is fed to both ridge limbs from a source located beneath the OSC. We conclude that the tectonic segmentation of the EPR as defined by OSCs is not the direct result of magmatic segmentation at mantle depths. Instead, the formation and general morphologic structure of OSCs may be controlled primarily by lithospheric processes, such as by instabilities in the local stress field (*10*) or by forces on the plate boundary that arise during changes in the spreading direction (*10, 12*). The right lateral offset of the 9°03′N OSC, similar to 10 of 11 other OSCs on the Pacific-Cocos plate boundary, suggests that the offset is formed in response to an anticlockwise change in the direction of spreading. Along this section of the EPR, a 3° to 6° anticlockwise change in the spreading direction is believed to have occurred within the past ~1 million years (*8, 9*).

References and Notes

1. P. Lonsdale, *J. Geophys. Res.* **88**, 9393 (1983).
2. K. C. Macdonald, P. J. Fox, *Nature* **302**, 55 (1983).
3. C. Langmuir, J. F. Bender, R. Batiza, *Nature* **322**, 422 (1986).
4. J. M. Sinton, S. Smaglik, J. J. Mahoney, K. C. Macdonald, *J. Geophys. Res.* **96**, 6133 (1991).
5. P. Lonsdale, *J. Geophys. Res.* **91**, 10493 (1986).
6. K. C. Macdonald, J.-C. Sempere, P. J. Fox, *J. Geophys. Res.* **91**, 10501 (1986).
7. K. C. Macdonald *et al.*, *Nature* **335**, 217 (1988).
8. S. M. Carbotte, K. C. Macdonald, *J. Geophys. Res.* **97**, 6959 (1992).
9. S. M. Carbotte, K. C. Macdonald, *J. Geophys. Res.* **99**, 13609 (1994).
10. K. C. Macdonald, D. S. Scheirer, S. M. Carbotte, *Science* **253**, 986 (1991).
11. H. Schouten, K. D. Klitgord, J. A. Whitehead, *Nature* **317**, 225 (1985).
12. P. Lonsdale, *J. Geophys. Res.* **94**, 713 (1989).
13. K. C. Macdonald *et al.*, *Mar. Geophys. Res.* **14**, 299 (1992).
14. J.-C. Sempere, K. C. Macdonald, *Tectonics* **5**, 881 (1986).
15. G. A. Barth, J. C. Mutter, *J. Geophys. Res.* **101**, 17951 (1996).
16. G. M. Kent, A. J. Harding, J. A. Orcutt, *J. Geophys. Res.* **98**, 13971 (1993).
17. G. M. Kent *et al.*, *Nature* **406**, 614 (2000).
18. The instrument array consisted of eight Office of Naval Research, ocean-bottom seismographs equipped with 1-Hz geophones and seven ocean-bottom hydrophone instruments, both from the Woods Hole Oceanographic Institution. The instruments were deployed for 3 to 5 days and recorded continuously at a 128-Hz sampling rate, during which time the R/V *Ewing*'s 20-gun, 8500-cubic-inch (139 liter) air gun array was fired along the tracks indicated in Fig. 1. A linear correction was applied to the time base of the data to account for clock drift (largest drift was <10 ms). Bathymetry data collected during the experiment was merged with older data (*13*) to reduce errors in the ray tracing calculations. Seafloor locations of the instruments were determined from shot positions and water-wave travel times (*39*).
19. Uncertainties in the travel-time picks are 11 ms for *Pg*, 14 ms for *PmP*, and 16 ms for *Pn*. Other experimental uncertainties (timing, instrument and shot location, bathymetry, and ray tracing) provide a combined uncertainty of about 8 ms. Therefore, the total uncertainty of the *Pn* data is ~18 ms.
20. J. P. Canales *et al.*, *Eos* (*Fall Suppl.*) **80**, F995 (1999).
21. Along-axis profiles of the Moho structure from (*20*) were applied to the east and west sides of the model. The profiles were then linearly interpolated across the rise.
22. H. H. Hess, *Nature* **203**, 629 (1964).
23. S. Zhang, S. Karato, *Nature* **375**, 774 (1995).
24. D. R. Toomey, S. C. Solomon, G. M. Purdy, *J. Geophys. Res.* **99**, 24135 (1994).
25. R. A. Dunn, D. R. Toomey, *Nature* **388**, 259 (1997).
26. _____, S. C. Solomon, *J. Geophys. Res.* **105**, 23537 (2000).
27. The model has dimensions of 44 km in *x* (perpendicular to the rise axis), 80 km in *y* (along the rise axis), and 11 km in *z* (vertical); the origin for *x* and *y* is the center of the experiment's planform: 9°0.42′N and 104°13.05′W. The model is parameterized in terms of isotropic and anisotropic (hexagonal symmetry system) slowness. For ray tracing, the grid spacing is 250 m and 200 m in the horizontal and vertical directions, respectively. The top of the model conforms to the seafloor and is overlain by a uniform-velocity water layer. The perturbation model for isotropic slowness is defined separately on a set of vertices within the three-dimensional volume used for ray tracing. In the crust, the grid spacing is set to 500 m in *x* and *y* and 200 m in *z*. In the mantle, the grid spacing is set to 1 km in *x*, *y*, and *z*. The perturbation model for anisotropic slowness (percent anisotropy and azimuth of the symmetry axis) is defined in the mantle region with a grid spacing of 2 km in the *x*, *y*, and *z* directions.
28. A similar misfit is obtained with less anisotropy (3 to 4% versus 6%) in a ~10-km-wide region centered beneath the rise (isotropic part of the model is not significantly different).
29. *Pn* travel times are relatively insensitive to small crustal thickness variations (*40, 41*). However, errors in the crustal thickness of the starting model may affect mantle imaging. We performed several tests to quantify the effect of any such errors. Synthetic data were generated for models with a constant velocity mantle and anomalous Moho structures; the synthetic data were then inverted for mantle velocity structure using a starting model with a flat Moho. No variations in the Moho depth were allowed, thus travel-time delays due to the prescribed Moho structure were mapped into mantle velocity structure. In some cases, the Moho structure consisted of four equally spaced regions of thickened crust centered beneath the rise axis (the anomalies were bell-shaped with diameters of 15 km). For 600-m depth anomalies, errors in the mantle velocity structure do not exceed 0.05 km s^{-1}, a value much less than the resolution of our tomographic images (~0.1 km s^{-1}). A depth error of 1.8 km is required to produce a 0.1 km s^{-1} error in the mantle velocity structure. For models with checkerboard patterns of Moho depth, anomalies had lengths of 5 to 10 km and Moho depths varied by ±500 m to ±900 m. Models with anomalies of less than ±800 m amplitude produced <0.1 km s^{-1} maximum error in the mantle images; models with ±800 to 900 m of Moho relief produced maximum errors of ~0.1 km s^{-1}. Smooth Moho structures (sine wave type versus square wave type) or smaller checks (5 km versus 10 km wide) had about 15 to 20% less effect on the mantle velocity structure. In other models where the anomalous Moho structure was located just where the *Pn* rays enter the mantle (three equally spaced 10 km by 15 km regions with a 600-m depth anomaly located off-axis on each side of the rise, and not within 12 km of the rise), errors in subaxial mantle imaging did not exceed ±0.03 km s^{-1} and thus insignificantly affect mantle imaging. The tests indicate that crustal thickness errors may affect mantle imaging at the 0.1 km s^{-1} level if the anomalous Moho structure is ≥10 km in lateral extent with a depth magnitude of ≥1.6 km. However, expected uncertainties in our crustal thickness estimate are less than ±500 m over such distances (*15, 20*) and thus produce a negligible error (<0.05 km s^{-1}) in the mantle images.
30. J. Madsen, R. Detrick, J. Mutter, P. Buhl, J. Orcutt, *J. Geophys. Res.* **95**, 4967 (1990).
31. J. Phipps Morgan, Y. J. Chen, *J. Geophys. Res.* **98**, 6283 (1993).
32. U. H. Faul, D. R. Toomey, H. S. Waff, *Geophys. Res. Lett.* **21**, 29 (1994).
33. D. R. Toomey, G. M. Purdy, S. C. Solomon, *Nature* **347**, 639 (1990).
34. S. C. Singh, G. M. Kent, J. S. Collier, A. J. Harding, J. A. Orcutt, *Nature* **394**, 874 (1998).
35. R. Haymon *et al.*, *Earth Planet. Sci. Lett.* **104**, 513 (1991).
36. S.-M. Lee, S. C. Solomon, M. A. Tivey, *J. Geophys. Res.* **101**, 22033 (1996).
37. S.-M. Lee, thesis, Massachusetts Institute of Technology/Woods Hole Oceanographic Institute, Woods Hole, MA (1995).
38. S. Bazin *et al.*, *Eos* (*Fall Suppl.*) **81**, F1346 (2000).
39. K. C. Creager, L. M. Dorman, *J. Geophys. Res.* **87**, 8379 (1982).
40. V. Cerveny, R. Ravindra, *Theory of Seismic Head Waves* (Univ. of Toronto Press, Toronto, 1971).
41. T. M. Hansen, S. C. Singh, B. H. Jacobsen, *Geophys. Res. Lett.* **26**, 2573 (1999).

42. We thank the officers and crew of the R/V *Ewing* and the Computational Research Institute at the University of Oregon for their assistance and resources. Critical reviews from K. Macdonald and an anonymous reviewer significantly improved this paper. This research was supported by the NSF.

22 November 2000; accepted 8 February 2001